Published in final edited form as:

IEEE Trans Biomed Eng. 2022 April ; 69(4): 1481–1490. doi:10.1109/TBME.2021.3120919.

Transcranial Theranostic Ultrasound for Pre-Planning and Blood-Brain Barrier Opening: A Feasibility Study using an Imaging Phased Array in Vitro and in Vivo

Alec J. Batts[1], **Robin Ji**[1], **Alina R. Kline-Schoder**[1], **Rebecca L. Noel**[1], **Elisa E. Konofagou**[1,2]

[1]Department of Biomedical Engineering, Columbia University, New York, USA

[2]Department of Radiology, Columbia University, New York, USA

Abstract

Focused ultrasound (FUS) for blood-brain barrier (BBB) opening is a safe, reversible and non-invasive strategy for targeted drug delivery to the brain, however extensive pre-planning strategies are necessary for successful FUS-mediated BBB opening through the structurally complex primate skull.

Objective: This work aims to demonstrate a pre-planning pipeline consisting of transcranial simulations and *in vitro* experimentation used to inform synchronous BBB opening and power cavitation imaging (PCI) with a single theranostic ultrasound (TUS) phased array.

Methods: Acoustic wave propagation simulation readouts of pressure attenuation and focal shift through clinical-CT and micro-CT-based primate skull models were compared, while the latter were used to determine the impact of beam steering angle on focal shift and pressure attenuation. *In vitro* experimentation with a channel phantom enabled characterization of skull-induced receive focal shift (RFS), while *in vivo* BBB opening and PCI using *in silico* and *in vitro* pre-planning information was conducted using a custom Verasonics/MATLAB script.

Results: Simulations confirmed steering angle dependent transcranial focal shift and pressure attenuation, while *in vitro* experiments revealed minimal (0.30–1.50 mm) skull-induced RFS. *In vivo* rodent experiments with overlaid primate skull fragments demonstrated successful TUS-mediated BBB opening and spatially correlated power cavitation images (PCI) with regions of BBB opening on T_1-weighted magnetic resonance images (MRI).

Conclusion: Herein, we demonstrate the feasibility for TUS-mediated BBB opening *in vivo* using *in silico* and *in vitro* pre-planning information.

Significance: TUS as an ultrasound-guided modality for BBB opening could be a promising alternative to current FUS-mediated BBB opening configurations in the clinic.

Corresponding author: Elisa E. Konofagou is with the Departments of Biomedical Engineering and Radiology, Columbia University, New York, NY 10032 USA (ek2191@columbia.edu).

Alec J. Batts, Robin Ji, Alina R. Kline-Schoder, and Rebecca L. Noel are with the Department of Biomedical Engineering, Columbia University.

Keywords

cavitation mapping; focused ultrasound; micro-CT; phased array; theranostic; transcranial ultrasound

I. Introduction

FOCUSED ultrasound (FUS)-induced blood-brain barrier (BBB) opening in conjunction with systemically administered microbubbles is a noninvasive, reversible and safe strategy for delivering therapeutics to the brain parenchyma in a targeted manner. Clinical progress has accelerated in recent years, with a large focus towards development of FUS-mediated BBB opening systems with treatment monitoring and guidance achieved with magnetic resonance imaging (MRI). Such MR-guided FUS (MRgFUS) BBB opening clinical trials have demonstrated BBB permeabilization in patients with Alzheimer's Disease (AD) [1], [2], amyotrophic lateral sclerosis (ALS) [3], brain tumors [4], and other neurological pathologies. While MRgFUS systems constitute the majority of clinical systems to date, development of ultrasound-guided techniques (USgFUS) poses low cost, high portability advantages over MR alternatives [5]. Furthermore, the added benefit of monitoring cavitation activity, understood to be the primary mechanism for FUS-mediated BBB opening with microbubbles [6], [7], along with the aforementioned cost and portability advantages, makes USgFUS a promising, translatable tool for the clinic.

Several preclinical and clinical ultrasound-based configurations have been investigated for monitoring BBB opening during treatment; many of these configurations rely on dual-transducer setups for simultaneous FUS administration and passive cavitation detection (PCD), commonly achieved with a single element transducer operated in receive-only mode, or passive acoustic mapping (PAM), enabled by beamforming techniques and multi-element linear or phased arrays. Several studies have utilized confocally aligned PCD [8]–[11] or PAM [12] with the FUS transducer for either real-time monitoring or off-line processing of cavitation induced by FUS. Other studies have utilized an off-axis configuration [11], [13]–[16], achieving a similar cavitation detection readout. Additionally, Liu *et al.* have designed and validated a multi-element FUS transducer configuration which achieves FUS-mediated BBB opening and cavitation monitoring from the same setup, albeit relying on off-line processing for reconstruction of cavitation maps [17], [18]. Our group has demonstrated initial feasibility of using a single diagnostic phased array, employed in a "theranostic" manner to achieve synchronous BBB opening and power cavitation imaging (PCI) [13], leveraging short pulses for high axial resolution cavitation maps [19]. This single array configuration poses a great potential for translation to the clinic given its highly portable nature and potentially improved user operability.

Regardless of the monitoring modality or configuration utilized for FUS-mediated BBB opening, *in silico* treatment pre-planning is almost ubiquitously used before treatment due to the complexity and variability of transcranial ultrasound transmission. Various components of the primate skull structure contribute to signal attenuation and beam distortion through distinct modes; while acoustic absorption primarily occurs in the dense cortical layers of the

skull [20], scattering effects induced by the irregular trabecular microstructure between these cortical layers also greatly contributes to the overall transcranial pressure loss and focal shift induced by the skull [20], [21]. Furthermore, our group has demonstrated the impact of the FUS beam incidence angle relative to the skull, underscoring the need for simulation-based pre-planning to maximize transcranial focal pressure [22].

In this study, we outline a pre-planning strategy which emphasizes skull microstructural information to achieve accurate *in silico* models of transcranial acoustic wave propagation while evaluating the advantages of using a single diagnostic phased array for synchronous transcranial BBB opening and PCI, a novel modality for BBB opening, coined herein as Theranostic Ultrasound (TUS). Using micro-CT information of primate skulls, we evaluate the impact of electronic beam steering enabled by the phased array on pressure attenuation and focal shift for the first time, in order to advantageously harness beam steering *in vivo*. We also determined the imaging registration error, or receive-mode focal shift (RFS), induced by the skull *in vitro* to evaluate the imaging accuracy of PCI in our TUS system [23]. Finally, we utilized this pre-planning information to inform transcranial, synchronized TUS-mediated BBB opening and PCI in mice with overlaid primate skull fragments, utilizing electronic beam steering to sonicate multiple targets.

II. Materials and Methods

A. Numerical simulations

Numerical transcranial acoustic wave propagation simulations were performed using the K-wave MATLAB toolbox [24], [25] to evaluate the impact of skull CT scan resolution and electronic beam steering angle on focal shift and pressure attenuation. A 96-element phased array (28.3 mm lateral, 16 mm elevational aperture size) with specifications based off of the P4–1 phased array transducer (ATL, Philips, Amsterdam, Netherlands) was reconstructed onto a 3D computational grid of axial, lateral and elevational dimensions of 400, 450 and 256 points, respectively, with 8 to 10 points/wavelength resolution as previously demonstrated to achieve convergence [26]. The resulting pressure distribution from a gaussian-enveloped 3-cycle pulse at a frequency of 1.5 MHz was evaluated in free field and through primate skull fragments consisting of frontal and parietal bone, whose density and sound speed maps were derived from either clinical-grade CT or micro-CT scans. Constant acoustic absorption was assumed for the whole fragment. Clinical CT scans were acquired with 0.488 mm and 0.250 mm isotropic resolution for human and NHP skull fragments, respectively, using a Siemens Biograph 64 clinical CT scanner (Siemens, Malvern, PA, USA), while micro-CT scans were acquired with 0.08 mm isotropic resolution for both human and NHP skull fragments using a MI Labs 3D optical CT scanner (MILabs, Netherlands). Hounsfield units were converted to density and sound speed as previously described [16], [27], and the resolution of the resulting material property maps were resampled to that of the computational grid. Density, sound speed and attenuation coefficient values for media surrounding the skull fragment were matched to that of water at 37 °C (1000 kg/m^3, 1524 m/s, and 3.5×10^{-4} dB/MHz. cm, respectively). For each simulation, the 3-cycle pulse emitted from the simulated P4–1 phased array focused at 35 mm, at 1.5 MHz and 1.0 MPa input peak-negative pressure (PNP) was permitted

to propagate for 90 μs (6,668 time steps, temporal resolution 1.35×10^{-8} s) leaving sufficient time for the ultrasound wave to travel to the edge of the computational grid and back to the transducer face. Six trials for each simulation were performed to account for experimental uncertainties by successively repositioning the skull maps relative to the array in the elevational dimension by 8 mm, corresponding to half of the elevational aperture dimension. The skull maps were fixed in the lateral and axial dimensions to maintain a normal incidence angle to the beam. Transcranial focal shift and attenuation were evaluated for each simulation by comparing the lateral coordinates, measured in the 2D imaging plane, and axial coordinates of the 0 dB focal point and PNP at the focal point through the skull to the resulting focal profile in free field. An analogous procedure was conducted to evaluate focal shift and attenuation dependence on electronic steering angle. Six trials for each steering angle ranging from 10° to +10° in 5° increments were conducted where the resulting center of the focus and attenuation were compared to the corresponding values simulated in free field. Simulations were run on a GPU (Quadro P5000, NVIDIA, Santa Clara, CA, USA) with an average computational time of ~35 minutes and ~48 minutes per free field and transcranial simulation, respectively.

B. Synchronous BBB opening and PCI Sequence

A diagnostic phased array (P4–1, ATL, Philips, Amsterdam, Netherlands) with a center frequency of 2.5 MHz (bandwidth: 1.5 MHz – 3.5 MHz, 96 elements) was operated by a research ultrasound system (Vantage 256, Verasonics Inc., Kirkland, WA, USA) at 1.5 MHz to achieve an optimal balance between transcranial ultrasound transmission and imaging resolution for all *in vitro* and *in vivo* experiments. A custom MATLAB script was developed using the Verasonics software package to perform BBB opening and PCI simultaneously using a single transducer [19]. In brief, 100 ~3-cycle focused transmits at a pulse repetition frequency (PRF) of 1,000 Hz were deployed at a set burst rate of 0.5 Hz, allowing for real time data processing, displaying, and saving. The Verasonics transmit structure enabled electronic focusing and steering of the beam by computing the appropriate element-wise time delays to achieve a given focal depth and steering angle. Received echoes were processed using the delay-and-sum beamforming method as described previously [13]. Furthermore, spatiotemporal clutter filtering of PCI was achieved using the singular value decomposition (SVD) as described by Demené *et al.* [28] to reduce skull signal contribution. In brief, received RF data from each burst was transformed into Casorati matrix form before calculating the SVD of the resulting covariance matrix. The eigenvectors corresponding to singular values below a predefined fixed cutoff value were discarded to increase the sensitivity of cavitation signals emanating from beneath the skull before reshaping the filtered data to its original form. Optimal singular value cutoffs were selected by minimizing the ratio between signal arising from the skull and microbubble oscillations. A total of 60–70 sets of 100 focused transmits followed by passive reception of acoustic emissions and SVD filtering were deployed for a total sonication duration of ~2 minutes for *in vivo* experiments. The singular value cutoff could also be modified when reprocessing the PCI data. The mean PCI generated from 60–70 frames of individual PCI was used for focal shift calculations and image registration as described in subsequent sections.

C. Microbubbles

In-house-made polydisperse microbubbles were manufactured according to previously published protocols [29], [30]. In brief, 1,2-distearoyl-sn-glycero-3-phosphocholine (DSPC, Avanti Polar Lipids Inc., Alabaster, AL, USA) and 1,2-distearoyl-sn-glycero-3-phosphoethanolamine-N-[methoxy(polyethylene glycol)-2000] (DSPC-mPEG2000, Avanti Polar Lipids Inc., Alabaster AL, USA) were combined at a 9:1 molar ratio. The lipids were dissolved in a 50 mL solution of filtered phosphate-buffered saline (80% volume)/glycerol (10% volume)/propylene glycol (10% volume) and immersed in a sonication bath for 1 to 2 hours. Microbubbles were activated using a sonicator (Model 1510, Branson Ultrasonics, Danbury, CT, USA) with flowing perfluorobutane (PFB) gas (FluoroMed L.P., Round Rock, TX, USA) over the lipid solution and stored in a glass vial at 4 °C. After aliquoting into individual 5 mL vials, air was vacuumed out and replaced with PFB repeatedly for a total of 5 times. Following PFB gas infusion, the vial was activated via a shaker (VialMix™, Lantheus Medical Imaging, N. Billerica, MA, USA) for 45 s.

D. In vitro TUS characterization

A series of *in vitro* experiments were conducted to evaluate both the expected focal shift and pressure attenuation through primate skulls and to determine the transcranial PCI receive-mode focal shift (RFS) induced by the skull. Skull fragments were submersed in partially degassed water, placed in a vacuum chamber, and were degassed for ~24 hours by removing all air from the chamber using a vacuum pump. Fragments were allowed to remain under maximum vacuum overnight with the pump turned off, after which, remaining gas bubbles were removed with the vacuum pump turned on for several hours the following day. Transcranial focal shift and pressure attenuation were evaluated in a degassed water tank with a needle hydrophone (HNP-0200, Onda Corp., Sunnyvale, CA, USA) as shown in Fig. 1A. The hydrophone affixed to a three-axis positioning system (BiSlide, Velmex Inc., Bloomfield, NY, USA) was translated in raster scan mode with 0.1 mm resolution and 20 mm axial × 10 mm lateral range to capture the focal area of the P4–1 with and without skull interference for both NHP and human skull fragments of 3.20 ± 0.42 mm and 5.38 ± 1.43 mm average thicknesses, respectively. Given that a 90° incidence angle of the beam to the skull was expected to yield the lowest relative pressure attenuation, skull fragments were positioned as perpendicular to the beam as possible [22]. Axial and lateral focal shifts were determined by comparison between the location of the 0 dB focal point after skull transmission and the location of the focal point without skull interference. Furthermore, skull-induced pressure attenuation was calculated as a percent of PNP lost after transcranial transmission relative to the PNP without the skull for a given input voltage.

A second *in vitro* experiment was performed in order to determine the RFS induced by the skull, with a setup inspired by a study conducted by Soulioti *et al.* [31]. The P4–1 was positioned 2–5 mm above the NHP and human skull fragments submerged in a degassed water bath (Fig. 1B). The water bath containing the skull was mounted above a small water tank containing a 254 μm-diameter flow channel, oriented orthogonally to the array's lateral dimension and positioned at a depth of approximately 35 mm from the transducer face, containing flowing in-house manufactured polydisperse, lipid-shelled microbubbles at a concentration of 8.0×10^8 MBs/mL continuously infused at set velocities of 2.3 to 8.9

mm/s by a syringe pump (Genie Plus, Kent Scientific, Torrington, CT, USA). A B-mode acquisition was obtained without skull interference to establish ground truth coordinates for the center of the flow channel. PCI performed in the manner described above was conducted with the skull positioned beneath the transducer at a perpendicular incidence angle to the beam. The first 5 and 10 singular values were discarded during SVD filtering of PCI for *in vitro* NHP and human skull experiments, respectively. Axial and lateral RFS were determined by comparison between the B-mode-acquired coordinates of the flow channel center and the point of highest signal intensity (0 dB) in the final PCI.

E. In vivo synchronous BBB opening and PCI with TUS

All murine studies were reviewed, approved by and performed in accordance with the Columbia University Institutional Animal Care and Use Committee. To evaluate transcranial BBB opening and PCI using TUS, the primate skull fragments were positioned at a normal incidence angle to the TUS beam in a degassed water bath situated atop male wild type C57BL/6J mice (Envigo, Indianapolis, IN, USA), and sonicated bilaterally using the BBB opening and PCI procedure described above (Fig. 1C). Mice were anesthetized with a mixture of oxygen and 1.0% to 2.0% vaporized isoflurane during the experiment and were restrained in a stereotaxic instrument (Model 900, David Kopf Instruments, Tujunga CA, USA) for the duration of the procedure. Depilatory cream was used to remove fur from the scalp before placing degassed ultrasound gel atop the mouse head to facilitate acoustic coupling. The P4–1 was positioned 2.3 mm anterior to lambda and centered laterally about the sagittal suture, situating the elevational dimension of the transducer parallel to the anterior/posterior dimension of the animal. A B-mode acquisition without a primate skull in place was acquired for PCI registration to contrast-enhanced MRI as discussed later. The skull was then placed over the mouse head and the TUS beam was electronically focused at 35 mm depth. Before sonication, the array was repositioned in the axial plane to compensate for axial focal shifts determined from pre-planning simulations. The beam was then laterally steered by 3.72° to sonicate each hemisphere of the brain for 120 seconds each, where each sonication was immediately preceded by a bolus injection of microbubbles (8.0×10^8 MBs/mL). A derated PNP of 450 kPa was used for these sonications, with a corresponding input voltage determined by the pressure attenuation values derived from simulation results and hydrophone measurements.

F. Magnetic Resonance Imaging

Contrast-enhanced MRI were acquired 30 minutes and 7 hours after TUS to confirm BBB opening, correlate regions of contrast-enhancement with PCI and evaluate BBB closure. Immediately after TUS, 0.2 mL of gadodiamide (Omniscan, GE Healthcare, Princeton NJ, USA) was delivered intraperitoneally and mice were placed in a 30 mm volume coil in the bore of a 9.4 T MRI system (Ascend, Bruker Medical, Billerica, MA, USA) for imaging with a T_1-weighted 2D FLASH sequence (TR: 230 ms, TE: 3.3 ms, Flip angle: 70°, 6 averages, FOV: 25.6 mm × 25.6 mm, Matrix size: 256 × 256, Slice thickness: 0.4 mm, Resolution 0.1 mm × 0.1 mm). A second injection of 0.2 mL of gadodiamide was injected ~6.5 hours after TUS to evaluate BBB opening reversibility with the same T_1-weighted sequence.

G. Histological Analysis

Approximately 24 hours after TUS exposure, mice were sacrificed by transcardial perfusion with PBS for 5 min followed by 4% paraformaldehyde (PFA) for 6 min. Mouse brains were then dissected, fixed in 4% PFA for 24 hours and transferred to 70% ethanol before sectioning and staining with hematoxylin and eosin (H&E) to assess safety of the TUS procedure. Four mouse brains were paraffin-embedded and coronally sectioned into 5-μm thick slices with 90 μm gaps between slices in the region of BBB opening. Bright-field microscopy with a 2.5x dry objective (Leica DM6 B, Leica Microsystems Inc., Buffalo Grove, IL, USA) was used to image the entire coronal slice. Images were evaluated for red blood cell (RBC) extravasation and damaged neurons in the region of BBB opening.

H. Image Analysis and Registration

PCI acquired *in vivo* were segmented based off of a B-mode acquisition of the murine skull before TUS and were manually registered to T_1-weighted MRI using a custom MATLAB script. Regions above a fixed threshold of gadolinium contrast enhancement on T_1-weighted MRI, indicating BBB opening, were compared with −6 dB regions of PCI via receiver-operating characteristic (ROC) analysis. Predictive ability of PCI for TUS-mediated BBB opening was assessed individually for each brain hemisphere in each animal by calculating the area under the curve (AUC) of each resulting ROC curve.

I. Statistical Analysis

All statistical analyses were conducted using GraphPad Prism (Version 8.30, GraphPad Software, San Diego, CA) and all measurements are presented as the mean ± standard deviation. Detailed descriptions of statistical tests used to analyze results are included in the corresponding figure caption. Transcranial acoustic wave propagation simulations were conducted for n=6 elevational transducer positions. *P* values reported are denoted as $^{**}p < 0.01$, $^{***}p < 0.001$, $^{****}p < 0.0001$ unless stated otherwise.

III. Results

A. High-resolution micro-CT-based skull models increased accuracy of attenuation measurements

Transcranial acoustic wave propagation simulations were conducted using the K-wave MATLAB toolbox to determine the effect of CT scan resolution on pressure attenuation and focal shift through primate skull fragments. Along with an observable fundamental increase in CT resolution (Fig. 2A–B), simulations revealed significantly increased attenuation measurements through both primate skulls using the micro-CT scan relative to the clinical CT scan (Fig. 2C–D), while only the NHP skull simulations exhibited significantly different focal shift (Fig. 2E). The micro-CT scan of the NHP skull fragment yielded an 85.1% increase in pressure attenuation relative to the clinical CT scan and an improvement in agreement with hydrophone determined measurements (74.3% attenuation) from 42.5% difference using the clinical CT to 1.9% difference using the micro-CT (Fig. 2C). Furthermore, a significantly reduced average axial shift of 0.5 mm was observed using the micro-CT compared to a 1.9 mm axial shift determined from the clinical CT (Fig.

2E). CT scan resolution did not significantly affect the lateral focal shift through the NHP skull. The micro-CT scan of the human skull fragment yielded a 10% increase in pressure attenuation relative to the clinical CT scan, an improvement in agreement with experimentally determined measurements (87,7% attenuation) from 12.0% difference to 5.1% difference (Fig. 2D). CT scan resolution did not significantly affect the axial or lateral focal shift of the TUS beam through the human skull fragment (Fig. 2F), though both models yielded focal shift values consistent with hydrophone-determined measurements (Fig. 2G–H).

B. Electronic beam steering increased transcranial pressure attenuation in an angle-dependent fashion

Given the improved accuracy of attenuation estimation using micro-CT data, subsequent transcranial acoustic wave propagation simulations were conducted using structural information derived from micro-CT scans. Simulations for both human and non-human primate skulls were carried out to determine the impact of electronic beam steering angle on transcranial pressure attenuation and focal shift (Fig. 3A–B). The simulated beam was steered from −10° to 10° in 5° intervals, yielding significantly reduced axial focal shift and pressure attenuation through the NHP skull with smaller steering angle magnitudes (Fig. 3C–D). A steering angle of +10° yielded an average attenuation of 76.4% ± 1.9% and axial focal shift magnitude of 6.63 mm ± 0.77 mm while a reduction to a 0° steering angle yielded 73.1% ± 0.9% attenuation and 0.56 mm ± 0.29 mm axial focal shift. No significant differences in lateral focal shift were observed as a result of varying the steering angle (Fig. 3C). An analogous set of simulations were performed for the human skull, and while no significant differences in pressure attenuation or focal shift were detected, greater variability in attenuation measurements was observed with increasing steering angle magnitude (Fig. 3E–F).

C. In vitro flow channel investigations confirmed minimal RFS

In order to determine the impact of the skull on PCI accuracy at the focus, a B-mode acquisition of a 0.254 mm diameter microbubble flow channel cross section was used to obtain ground truth coordinates for the center of the flow channel after which primate skull fragments were placed approximately 10 mm beneath the transducer face for transcranial PCI. The axial and lateral coordinates of the −6 dB center of the PCI of the flow channel were then compared to that of the B-mode image before the skull placement to determine the skull-induced receive-profile focal shift (RFS). The −6 dB center of the PCI through the NHP skull was shifted 1.50 mm axially and 0.90 mm laterally, while that of the PCI through the human skull was shifted 1.20 mm axially and 0.30 mm laterally (Fig. 4A–B). These results indicate that PCI spatial representation of cavitation activity is minimally affected by phase aberrations and focal distortion induced by the skull.

D. Bilateral BBB opening and PCI was achieved through primate skulls by electronically steering a single phased array

Using the pressure attenuation and focal shift information from both the micro-CT-based acoustic wave propagation simulations and experimental measurements with a hydrophone, while considering an expected RFS of 0.30–1.50 mm determined by the microbubble flow

channel experiments, bilateral transcranial BBB opening and PCI was achieved with a single phased array (Fig. 5A–B). Compensation for the axial focal shift observed in simulations (Fig. 3C,E) was performed by translating the transducer in the axial dimension by the average axial focal shift for a 3.72° steered transmit through each skull specimen. For NHP skull experiments, the transducer was shifted up (towards the skull) by 1.1 mm, while for human skull experiments, the transducer was shifted down (towards the skull) by 3.7 mm. For each experiment, a bolus injection of microbubbles was injected before sonication on the right hemisphere, followed by a second bolus injection of microbubbles and subsequent switching of the steering angle for sonication on the left hemisphere. High predictive ability of the −6 dB region of PCI acquired through the NHP skull was demonstrated by average AUC of 0.722 ± 0.068 and 0.744 ± 0.035 for openings on the left and right hemisphere, respectively (Fig. 5C–D). Acquired PCI maps through the human skull had average AUC values of for the left and right hemisphere of 0.824 ± 0.092 and 0.788 ± 0.037, respectively (Fig. 5C–D). These results provide further evidence of *in vivo* feasibility of transcranial BBB opening with TUS while demonstrating high classification-performing and spatially accurate PCI.

E. Safety and Reversal of TUS-mediated BBB opening

A second set of T_1-weighted MRI were acquired 7 hours after sonication to evaluate BBB reversibility after TUS in mice with both overlaid NHP and human skull fragments. Lack of detectable contrast enhancement above the threshold for BBB opening indicated that the openings were closed within 7 hours after TUS (Fig. 6A–B). Histological examination of H&E-stained coronal brain slices of mice with overlaid skull fragments confirmed absence of RBC extravasation within the TUS-exposed regions in both sonicated hemispheres, attesting to the safety of the TUS procedure used in this study (Fig. 6C–E).

IV. Discussion

Herein we demonstrated a pre-planning and treatment pipeline for synchronous transcranial BBB opening and PCI with a theranostic phased array. Micro-CT based simulations enabled more accurate prediction of pressure attenuation and focal shift through primate skulls relative to lower resolution clinical-CT based simulations. Furthermore, micro-CT based simulations also revealed steering-angle dependent pressure attenuation and focal shift information which was utilized for *in vivo* BBB opening treatment planning. We also evaluated the performance of the present PCI modality by assessing RFS of a microbubble flow channel *in vitro* induced by primate skulls; results indicated that such RFS were minimal and could be deemed negligible when registering PCI to areas of contrast enhancement on post-TUS T_1-weighted MRI *in vivo*. This collection of pre-planning material informed our *in vivo* investigation of synchronous BBB opening and PCI through primate skull fragments in which transcranial derated PNPs previously demonstrated to be safe [32]–[34] were used to transiently disrupt the BBB in mice using a single theranostic phased array with electronic beam steering. Spatial selectivity of PCI was demonstrated by high correlation between the −6 dB region of PCI and regions of gadolinium contrast enhancement on T_1-weighted MRI.

While micro-CT information yielded accurate pre-planning information in this murine study, micro-CT acquisitions pose obvious limitations when translated to larger animal or human studies. In order to achieve micrometer-size resolution, the small diameter of the bore in many micro-CT systems restricts specimens to small animals or small fragments of skull bone requiring the use of clinical CT systems for larger animals or humans. To provide clinically relevant micro-CT information for treatment planning in humans, studies investigating a relationship between CT scan resolution and pressure attenuation are ongoing. Robertson *et al.* have investigated the impact of CT scan image homogenization on acoustic transmission and time-of-flight supporting our claims that high resolution CT information is needed to resolve trabecular microstructure and capture scattering effects which dominate pressure attenuation at the TUS transmit center frequency of 1.5 MHz used in this study [35], [36].

Interestingly, even without taking into account shear wave and elastic considerations in our transcranial acoustic wave propagation simulations, the high-resolution microstructure information yielded attenuation measurements consistent with experimentally acquired data with a hydrophone. Though these simulations provided accurate information for the purposes of this study, acoustic simulations with micro-CT scans should be performed in conjunction with elastic modelling to determine the additional impact of this phenomenon on pressure attenuation and focal shift through primate skulls. These simulations also revealed a highly variable transmit-mode focal shift upon transcranial transmission. Interpreted from these results, focal shift is highly dependent on local skull geometry intersecting with the TUS beam and is challenging to simplify due to the highly complex geometrical and structural nature of primate skull bone. The impact of the discretization of CT scans, termed “staircasing” as described by Robertson *et al.* onto the computational grid may contribute to this variability in our simulations [26]. Furthermore, as registration of the clinical CT and micro-CT scans was carefully performed manually, registration errors between the two scans may also contribute to focal shifts observed in simulations. While preliminary insights are provided in this study, further investigations into the factors affecting transcranial TUS focal shift are ongoing.

Given the ability of the P4–1 diagnostic phased array to electronically steer the FUS beam, our micro-CT simulations were also utilized to determine the effect of steering angle on pressure attenuation and focal shift through primate skulls. While statistically significant increases in attenuation were observed with increasing beam steering angle magnitudes through the NHP skull fragments, no such differences were observed through the human skull, albeit with greater variability. We believe that this may be due to the increased heterogeneity in effective incidence angle between the skull and the beam with the generally reduced radius of curvature of the NHP skull relative to the human skull, but rigorous experimental and *in silico* assessments of skull geometrical considerations affecting focal shift are needed to confirm this hypothesis.

Along with numerical simulations, *in vitro* experiments used to determine the PCI RFS induced by the skull provided critical pre-planning information for our *in vivo* experiments. Minimal lateral and axial shifts of the PCI 0 dB focal area from the center of the B-mode image of a flow channel containing continuously flowing microbubbles, simulating a

cerebral vessel, revealed accurate spatial mapping of cavitation events beneath primate skull fragments. It is worth mentioning that the resolution limitation of TUS did yield uncertainty in estimating the center of the flow channel with PCI. While the 0 dB point within the −6dB region of PCI acquired of the channel phantom was chosen as the comparator to center coordinates of the channel in the B-mode acquisition, the −6 dB focal area encompassed an area much larger than the inner cross-sectional area of the channel depicted on the B-mode image, and that of the channel itself. However, since all calculated RFS values were below 1.50 mm, PCI is shown to be a robust tool for accurate spatial mapping of cavitation events, albeit limited by relatively poor lateral resolution.

While average AUC values indicated good agreement between the region of BBB opening on T_1-weighted MRI and focal regions of corresponding PCI, errors arising from manual registration of MRI and PCI along with an expected RFS of 0.30–1.50 mm as confirmed by *in vitro* flow channel experiments may minimally confound these results. Development of automated registration methods are ongoing and may improve these results.

Our *in vivo* study also elucidated important findings regarding the reversibility and safety of the TUS procedure described herein. All BBB openings were closed within 7 hours following TUS exposure as confirmed by contrast-enhanced T_1-weighted MRI which aligns with previous studies from our group indicating a closing period of 8 hours required for FUS-induced BBB openings with relatively short pulses (1.5 MHz center frequency, 67 μs pulse length, 450 kPa PNP) [34]. Given the substantially shorter pulse length of ~2 μs and analogous mechanical index (MI) employed in our TUS procedure relative to that of the aforementioned study, we expect BBB closing to occur at a slightly increased rate. Furthermore, another study employing short pulses to achieve a reduced duration of BBB permeability notes a further condensed BBB closing timeline on the order of several minutes as evaluated by permeability to 3.0 kDa fluorescently-tagged dextran (1.0 MHz, ~5 μs pulse length, 350 kPa PNP, 0.35 MI) [37]. Although the pulse length and MI used in our TUS procedure closely aligns with the ~5 μs pulse length and MI of 0.35 employed in [37], the closing timeline in our study was evaluated by contrast-enhanced T1-weighted MRI using a contrast agent with a molecular weight of 0.59 kDa. Given its reduced size relative to the 3.0 kDa dextran used in the aforementioned study, passage of the contrast agent across the disrupted BBB occurs for a longer period of time, contributing to the relatively longer closing timeline reported in our study. Further investigation into the effects of pulse length on TUS-mediated BBB opening permeability are ongoing.

Additional future directions include assessment of BBB opening permeability using dynamic contrast-enhanced MRI (DCE-MRI) and K_{trans} analysis to further characterize BBB opening induced by TUS.

V. Conclusion

In this study, valuable pre-planning information enabled by high resolution micro-CT scans and *in vitro* flow channel experiments was used to inform BBB opening and PCI with TUS. Bilateral sonications were achieved using electronic beam steering, a technique which may be employed in large animal models or clinically to induce BBB opening in multiple regions

of the brain with reduced treatment planning time. With ongoing further assessment of TUS capabilities to achieve tunable, controlled, and rapidly reversible BBB opening for delivery of therapeutics, TUS may be a promising alternative for MRgFUS in the clinic.

Acknowledgements

The authors wish to thank Akiva Mintz, MD, PhD and Andrei Molotkov, MD, PhD from the Columbia University PET Center for assistance with CT acquisitions as well as the Molecular Pathology/MPSR facility for histology services.

This manuscript was submitted for review on May 18, 2021. This work was supported in part by the National Institutes of Health under Grants R01AG038961 and R01EB009041, and by the Focused Ultrasound Foundation.

References

[1]. Lipsman N et al. , “Blood–brain barrier opening in Alzheimer’s disease using MR-guided focused ultrasound,” Nat. Commun, vol. 9, no. 1, Art. no. 1, Jul. 2018.

[2]. Mehta RI et al. , “Blood-Brain Barrier Opening with MRI-guided Focused Ultrasound Elicits Meningeal Venous Permeability in Humans with Early Alzheimer Disease,” Radiology, vol. 298, no. 3, pp. 654–662, Jan. 2021. [PubMed: 33399511]

[3]. Abrahao A et al. , “First-in-human trial of blood-brain barrier opening in amyotrophic lateral sclerosis using MR-guided focused ultrasound,” Nat. Commun., vol. 10, no. 1, Art. no. 1, Sep. 2019.

[4]. Mainprize T et al. , “Blood-Brain Barrier Opening in Primary Brain Tumors with Non-invasive MR-Guided Focused Ultrasound: A Clinical Safety and Feasibility Study,” Sci. Rep, vol. 9, no. 1, Art. no. 1, Jan. 2019.

[5]. Pouliopoulos AN et al. , “A Clinical System for Non-invasive Blood-Brain Barrier Opening Using a Neuronavigation-Guided Single-Element Focused Ultrasound Transducer,” Ultrasound Med. Biol, vol. 46, no. 1, pp. 73–89, Jan. 2020. [PubMed: 31668690]

[6]. Konofagou EE et al. , “Ultrasound-Induced Blood-Brain Barrier Opening,” Curr. Pharm. Biotechnol, vol. 13, no. 7, pp. 1332–1345, Jun 2012. [PubMed: 22201586]

[7]. Burgess A and Hynynen K, “Noninvasive and Targeted Drug Delivery to the Brain Using Focused Ultrasound,” ACS Chem. Neurosci, vol. 4, no. 4, pp. 519–526, Jan. 2013. [PubMed: 23379618]

[8]. Wu S-Y et al. , “Characterizing Focused-Ultrasound Mediated Drug Delivery to the Heterogeneous Primate Brain In Vivo with Acoustic Monitoring,” Sci. Rep, vol. 6, Nov. 2016.

[9]. McDamrold N et al. , “Targeted disruption of the blood-brain barrier with focused ultrasound: association with cavitation activity,” Phys. Med. Biol, vol. 51, no. 4, pp. 793–807, Feb. 2006. [PubMed: 16467579]

[10]. Chen H and Konofagou EE, “The size of blood-brain barrier opening induced by focused ultrasound is dictated by the acoustic pressure,” J. Cereb. Blood Flow Metab. Off. J. Int. Soc. Cereb. Blood Flow Metab, vol. 34, no. 7, pp. 1197–1204, Jul. 2014.

[11]. Kamimura HAS et al. , “Real-Time Passive Acoustic Mapping Using Sparse Matrix Multiplication,” IEEE Trans. Ultrason. Ferroelectr. Freq. Control, vol. 68, no. 1, pp. 164–177, Jan. 2021. [PubMed: 32746182]

[12]. Yang Y et al. , “Cavitation dose painting for focused ultrasound-induced blood-brain barrier disruption,” Sci. Rep, vol. 9, Feb. 2019.

[13]. Burgess MT et al. “Power cavitation-guided blood-brain barrier opening with focused ultrasound and microbubbles,” Phys. Med. Biol, vol. 63, no. 6, p. 065009, Mar. 2018. [PubMed: 29457587]

[14]. Choi JJ et al. , “Non-invasive and real-time passive acoustic mapping of ultrasound-mediated drug delivery,” Phys. Med. Biol, vol. 59, no. 17, pp. 4861–4877, Aug. 2014. [PubMed: 25098262]

[15]. Haworth KJ et al. , “Trans-Stent B-Mode Ultrasound and Passive Cavitation Imaging,” Ultrasound Med. Biol, vol. 42, no. 2, pp. 518–527, Feb. 2016. [PubMed: 26547633]

[16]. Wu S-Y et al. , “Efficient Blood-Brain Barrier Opening in Primates with Neuronavigation-Guided Ultrasound and Real-Time Acoustic Mapping,” Sci. Rep, vol. 8, no. 1, Art. no. 1, May 2018.

[17]. Liu H-L et al. , “Design and Experimental Evaluation of a 256-Channel Dual-Frequency Ultrasound Phased-Array System for Transcranial Blood-Brain Barrier Opening and Brain Drug Delivery,” IEEE Trans. Biomed. Eng, vol. 61, no. 4, pp. 1350–1360, Apr. 2014. [PubMed: 24658258]

[18]. Liu H-L et al. , “Design and Implementation of a Transmit/Receive Ultrasound Phased Array for Brain Applications,” IEEE Trans. Ultrason. Ferroelectr. Freq. Control, vol. 65, no. 10, pp. 1756–1767, Oct. 2018. [PubMed: 30010555]

[19]. Ji R et al. , “Transcranial Blood-Brain Barrier Opening and Power Cavitation Imaging Using a Diagnostic Imaging Array,” in 2019 IEEE International Ultrasonics Symposium (IUS), Oct. 2019, pp. 2–4.

[20]. Pinton G et al. , “Attenuation, scattering, and absorption of ultrasound in the skull bone,” Med. Phys, vol. 39, no. 1, pp. 299–307, 2012. [PubMed: 22225300]

[21]. Chaffaí S et al. , “Ultrasonic characterization of human cancellous bone using transmission and backscatter measurements: relationships to density and microstructure,” Bone, vol. 30, no. 1, pp. 229–237, Jan. 2002. [PubMed: 11792590]

[22]. Karakatsani MEM et al. , “Targeting Effects on the Volume of the Focused Ultrasound-Induced Blood-Brain Barrier Opening in Nonhuman Primatesln Vivo,” IEEE Trans. Ultrason. Ferroelectr. Freq. Control, vol. 64, no. 5, pp. 798–810, May 2017. [PubMed: 28320656]

[23]. Batts A and Konofagou E, “Targeting Accuracy of Transcranial Power Cavitation Imaging for Blood-Brain Barrier Opening Using a Theranostic Phased Array, ” in 2020 IEEE International Ultrasonics Symposium (IUS), Sep. 2020, pp. 1–3.

[24]. Treeby BE and Cox BT, “k-Wave: MATLAB toolbox for the simulation and reconstruction of photoacoustic wave fields,” J. Biomed. Opt, vol. 15, no. 2, p. 021314, Apr. 2010. [PubMed: 20459236]

[25]. Treeby BE et al. , “Modeling nonlinear ultrasound propagation in heterogeneous media with power law absorption using a k-space pseudospectral method,” J. Acoust. Soc. Am, vol. 131, no. 6, pp. 4324–4336, Jun. 2012. [PubMed: 22712907]

[26]. Robertson JLB et al. , “Accurate simulation of transcranial ultrasound propagation for ultrasonic neuromodulation and stimulation,” J. Acoust. Soc. Am, vol. 141, no. 3, pp. 1726–1738, Mar. 2017. [PubMed: 28372121]

[27]. Aubry J-F et al. , “Experimental demonstration of noninvasive transskull adaptive focusing based on prior computed tomography scans,” J. Acoust. Soc. Am, vol. 113, no. 1, pp. 84–93, Jan. 2003. [PubMed: 12558249]

[28]. Demené C et al. , “Spatiotemporal Clutter Filtering of Ultrafast Ultrasound Data Highly Increases Doppler and fUltrasound Sensitivity,” IEEE Trans. Med. Imaging, vol. 34, no. 11, pp. 2271–2285, Nov. 2015. [PubMed: 25955583]

[29]. Feshitan JA et al. , “Microbubble size isolation by differential centrifugation,” J. Colloid Interface Sci, vol. 329, no. 2, pp. 316–324, Jan. 2009. [PubMed: 18950786]

[30]. Wang S et al. , “Microbubble Type and Distribution Dependence of Focused Ultrasound-Induced Blood–Brain Barrier Opening,” Ultrasound Med. Biol, vol. 40, no. 1, pp. 130–137, Jan. 2014. [PubMed: 24239362]

[31]. Soulioti DE et al. , “Super-resolution imaging through the human skull,” IEEE Trans. Ultrason. Ferroelectr. Freq. Control, pp. 1–1, 2019.

[32]. Choi JJ et al. , “Noninvasive and localized blood-brain barrier disruption using focused ultrasound can be achieved at short pulse lengths and low pulse repetition frequencies,” J. Cereb. Blood Flow Metab. Off. J. Int. Soc. Cereb. Blood Flow Metab, vol. 31, no. 2, pp. 725–737, Feb. 2011.

[33]. Tung Y-S et al. , “In vivo transcranial cavitation threshold detection during ultrasound-induced blood–brain barrier opening in mice,” Phys. Med. Biol, vol. 55, no. 20, pp. 6141–6155, Oct. 2010. [PubMed: 20876972]

[34]. Samiotaki G and Konofagou EE, “Dependence of the reversibility of focused- ultrasound-induced blood-brain barrier opening on pressure and pulse length in vivo,” IEEE Trans. Ultrason. Ferroelectr. Freq. Control, vol. 60, no. 11, pp. 2257–2265, Nov. 2013. [PubMed: 24158283]

[35]. Robertson J et al. , “The effects of image homogenisation on simulated transcranial ultrasound propagation,” Phys. Med. Biol, vol. 63, no. 14, p. 145014, Jul. 2018. [PubMed: 29897047]

[36]. White DN et al. , “The acoustic characteristics of the skull,” Ultrasound Med. Biol, vol. 4, no. 3, pp. 225–252, Jan. 1978. [PubMed: 751304]

[37]. Morse SV et al. , “Rapid Short-pulse Ultrasound Delivers Drugs Uniformly across the Murine Blood-Brain Barrier with Negligible Disruption,” Radiology, vol. 291, no. 2, pp. 459–466, Mar. 2019. [PubMed: 30912718]

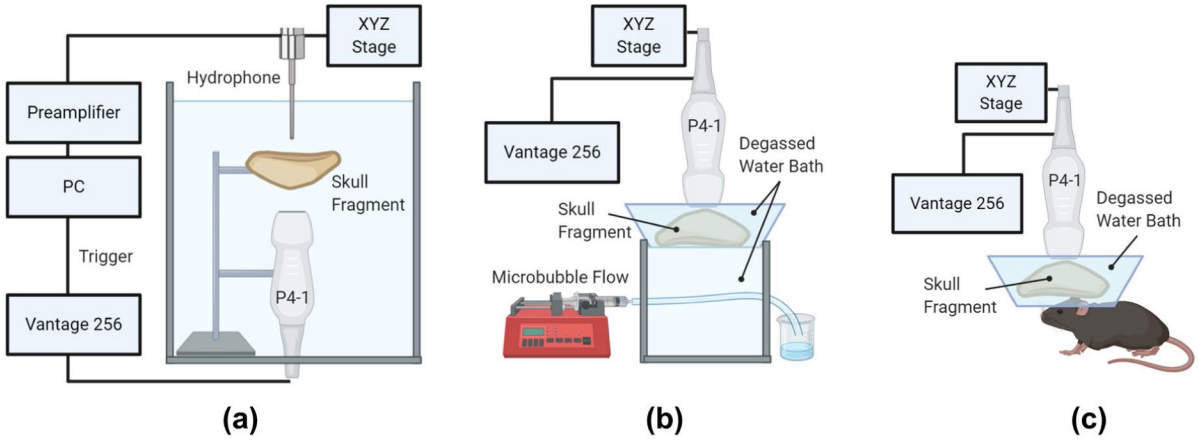

Fig. 1.

Experimental setup for **(a)** transcranial pressure attenuation measurements, **(b)** *in vitro* PCI RFS calculations and **(c)** *in vivo* synchronous TUS-mediated BBB opening and PCI. Figure created using Biorender.

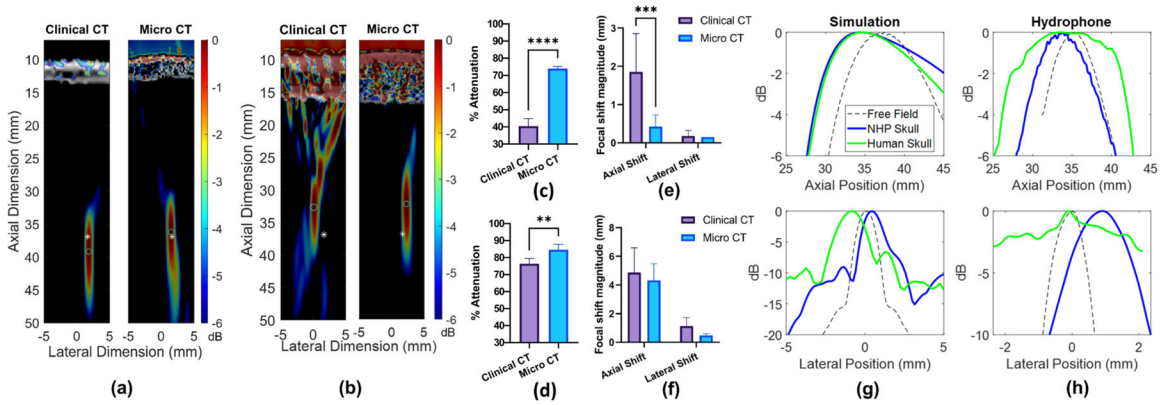

Fig. 2.

Simulated −6 dB focal regions through clinical CT vs micro-CT scans of an **(a)** NHP skull fragment and **(b)** a human skull fragment. White asterisks and cyan circles denote the 0 dB center of the focus simulated in free field, and through skulls, respectively. dB scale on color bar is self-normalized for each pressure plot. **(c)** A significant increase in pressure attenuation through an NHP skull fragment was observed in the simulation using a micro-CT compared to the clinical CT scan (****p<0.0001). **(d)** A significant increase in pressure attenuation through the human skull fragment was also observed using the micro-CT compared to the clinical CT scan (**p<0.01). **(e)** A significant decrease in axial focal shift was observed in the micro-CT simulation relative to the clinical CT simulation (**p<0.01) for the NHP skull, while **(f)** no statistically significant differences in focal shift were observed for the human skull. These results were determined by an unpaired Student's t-test with n=6 lateral/elevational transducer positions. **(g)** Axial (top) and lateral (bottom) simulated focus profiles in free field (dashed line), through NHP skull, and human skull using micro-CT scans shown in (a-b). **(h)** Experimentally-determined axial (top) and lateral (bottom) focus profiles in free field, through NHP skull, and human skull.

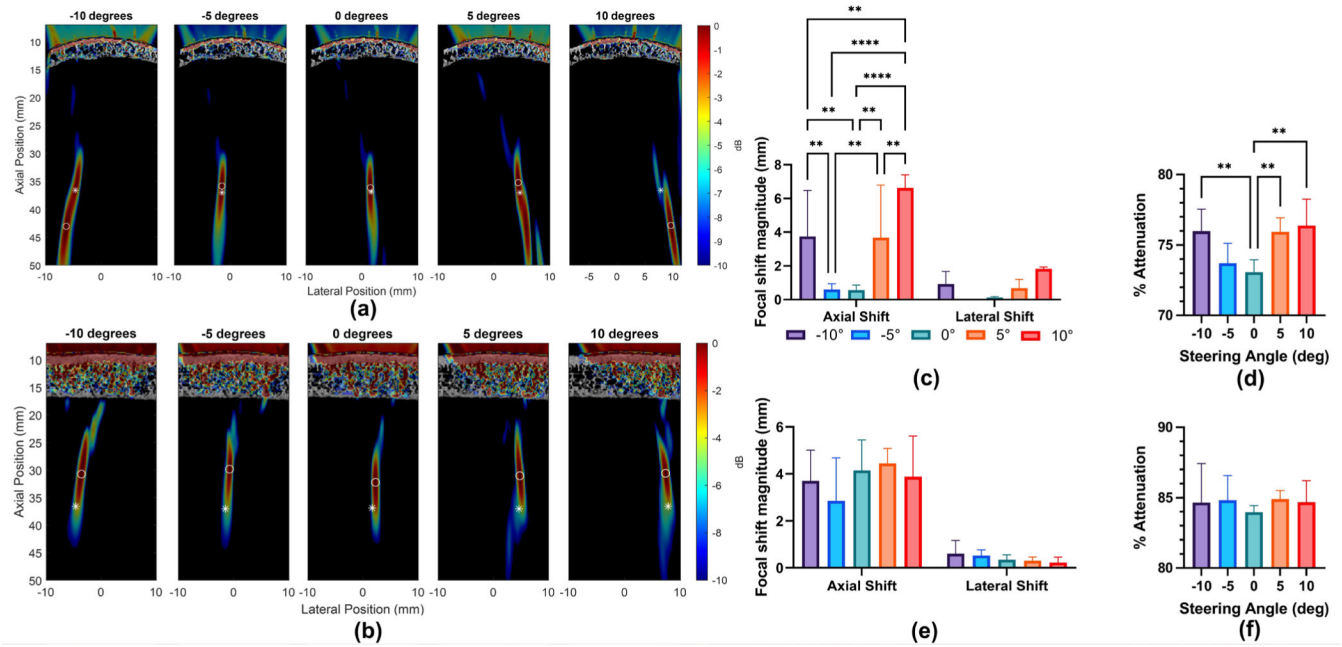

Fig. 3.

Simulated impact of steering angle on pressure attenuation and focal shift. −6 dB focal regions of simulated focused transmits with varying steering angles through the **(a)** NHP skull and **(b)** human skull. Asterisk denotes center of the focus in free field, while circle denotes center of the focus after transcranial transmission. dB scale on color bar is self-normalized for each pressure plot. Steering angle dependent focal shift and attenuation through the NHP skull **(c-d)** and human skull fragment **(e-f)**. Statistical significance determined by one-way ANOVA with post-hoc Tukey's multiple comparisons test where, ** $p<0.01$, *** $p<0.001$. **** $p<0.0001$, for n=6 simulation trials.

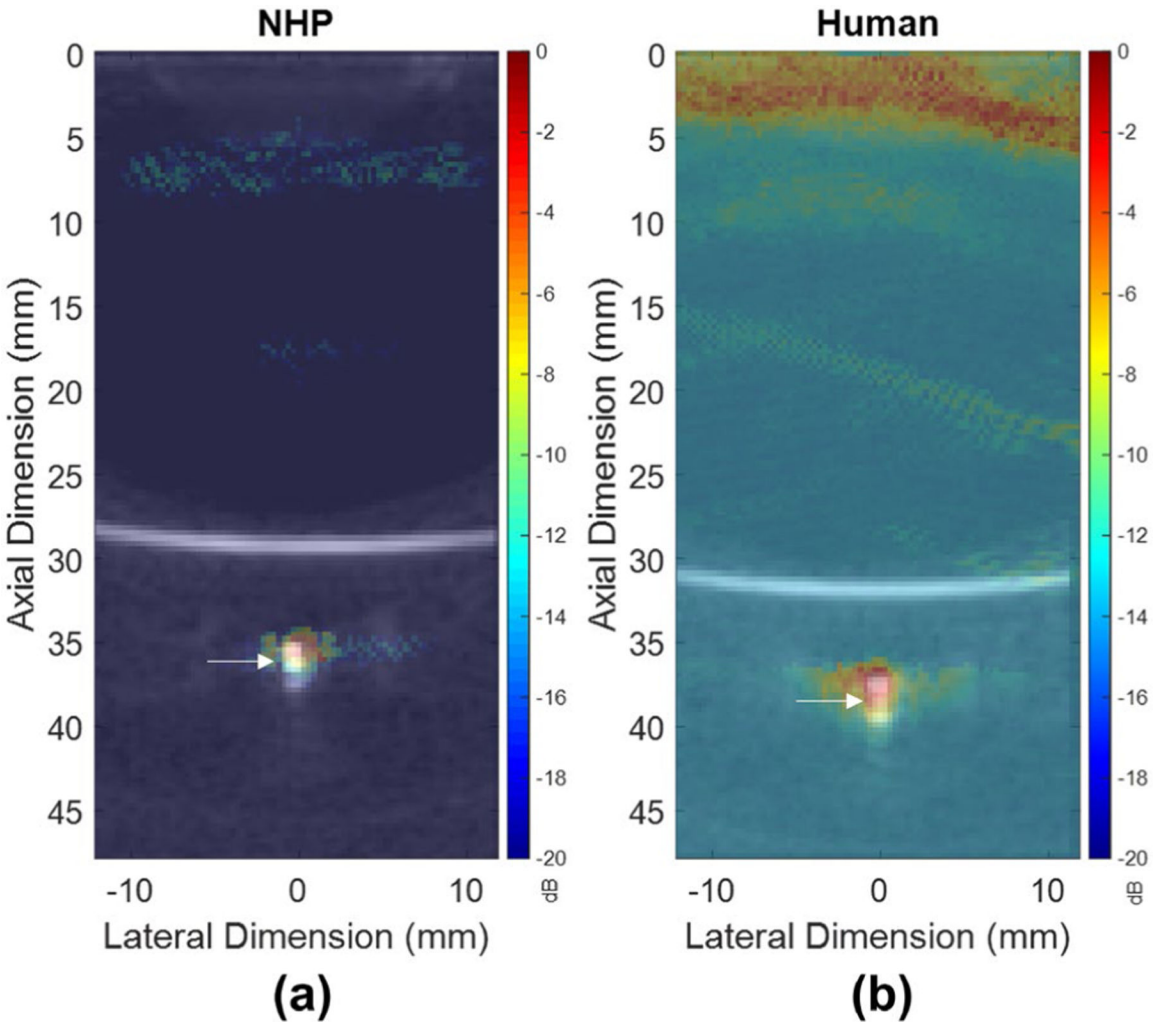

Fig. 4.

Transcranially-acquired PCI with overlaid B-mode images acquired of the channel phantom without skull interference for the **(a)** NHP skull, and **(b)** human skull, utilized to determine RFS. White arrows denote the center of the channel phantom on B-mode acquisitions.

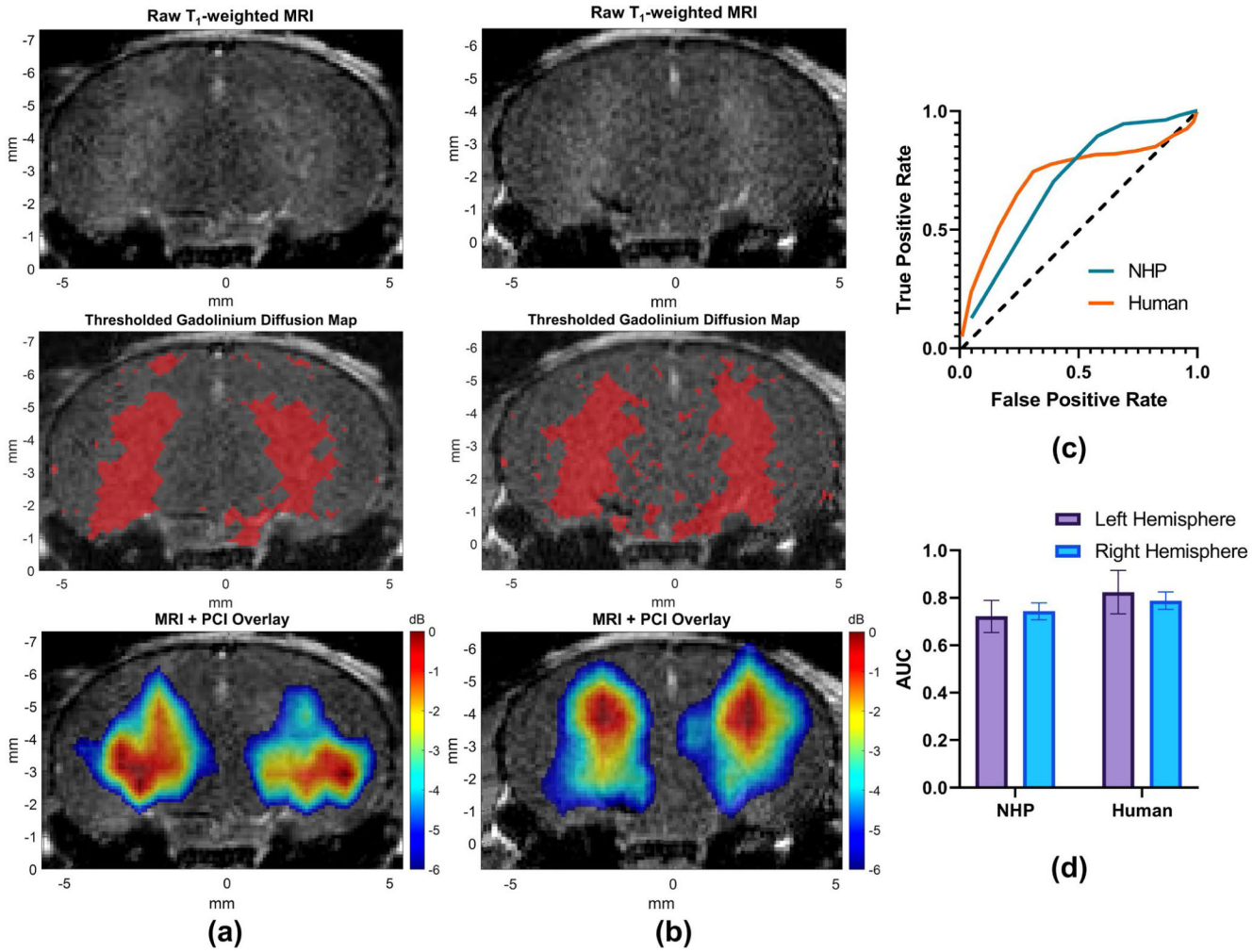

Fig. 5.

In vivo BBB opening and PCI. Raw contrast enhanced T_1-weighted MRI (top panel) for **(A)** NHP skull and **(B)** human skull fragments. Thresholded regions of contrast enhancement used for ROC analysis with PCI (middle panel). Overlaid −6 dB focal regions of PCI (bottom panel) for **(A)** NHP skull and **(B)** human skull fragments. **(C)** Representative receiver operator characteristic (ROC) curves demonstrating correlation between contrast-enhanced regions of T_1-weighted MRI and −6 dB focal regions of PCI. **(D)** Area under the curve (AUC) for n=4 mice per group. Error bars denote the mean ± standard deviation.

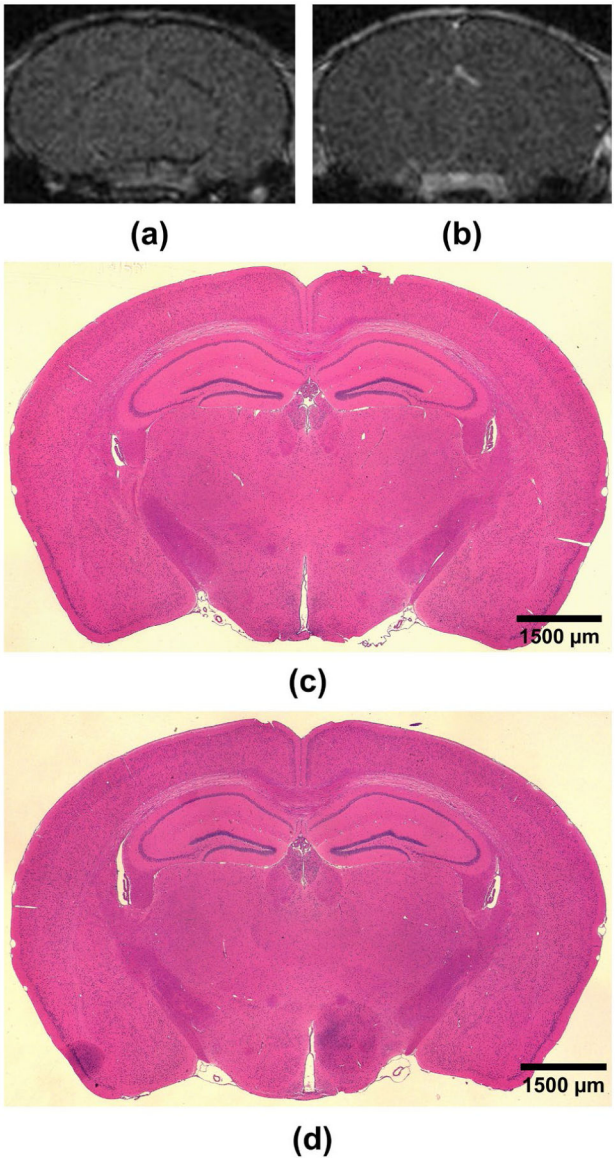

Fig. 6.

Reversibility and safety of TUS-mediated BBB opening. Representative T_1-weighted MRI acquired 7 hours after TUS for **(A)** NHP skull and **(B)** human skull sonications depicting lack of contrast enhancement in regions of BBB opening (in Fig. 5A-B). Representative coronal H&E-stained brain slices of mouse brains sonicated bilaterally with an overlaid NHP skull fragment (C) or human skull fragment (D). No signs of damage were observed in any H&E-stained brain sections. Scale bars denote 1500 μm.